Surfaces and Interfaces 77 (2025) 108023

Contents lists available at ScienceDirect

Surfaces and Interfaces

journal homepage: www.sciencedirect.com/journal/surfaces-and-interfaces

Halloysite-based multifunctional filler for antibacterial and anticorrosive protective coatings: a sustainable approach using kojic acid and ionic liquids

Erika Saccullo [a,b,1], Angelo Ferlazzo [c,1], Virginia Fuochi [b], Salvatore Furnari [b], Rosamaria Lombardo [a], Luca Spitaleri [d], Gianfranco Sfuncia [e], Giuseppe Nicotra [e], Pio Maria Furneri [b], Antonino Gulino [c], Rosario Pignatello [a,f], Antonio Rescifina [a,f], Vincenzo Patamia [a,f,*], Giuseppe Floresta [a,f,*]

[a] Department of Drug and Health Sciences, University of Catania, Viale Andrea Doria 6 95125 Catania, Italy
[b] Department of Biomedical and Biotechnological Sciences (Biometec), University of Catania, Via Santa Sofia 97 95123 Catania, Italy
[c] Department of Chemical Sciences, University of Catania, Viale Andrea Doria 6 95125 Catania, Italy
[d] STMicroelectronics Stradale Primosole, 50 95121 Catania, Italy
[e] Institute for Microelectronics and Microsystems CNR-IMM, Zona Industriale Strada VIII, 5 95121 Catania, Italy
[f] NANOMED—Research Centre for Nanomedicine and Pharmaceutical Nanotechnology, University of Catania 95125, Catania, Italy

ARTICLE INFO

Keywords:
Halloysite
Kojic acid
Chelating agent
Sustainable material
Smart material

ABSTRACT

In this study, we present a novel multifunctional filler for protective coatings, highlighting its straightforward and rapid synthesis. This composite is based on halloysite nanotubes (HNTs), a naturally occurring clay mineral, covalently functionalized with kojic acid (K), a naturally occurring chelating agent. This unique combination offers powerful antibacterial and anticorrosive properties. The kojic acid-functionalized halloysite nanotubes (HNT-K) were then loaded with an ionic liquid (IL), leveraging synergistic interactions to effectively inhibit iron oxidation and provide robust surface protection. The composite underwent comprehensive characterization through Fourier-transform infrared spectroscopy (FTIR), X-ray photoelectron spectroscopy (XPS), Transmission electron microscopy (TEM), and Linear Polarization Resistance (LPR) analyses, which unequivocally confirmed successful functionalization and loading, along with a significant improvement in both corrosion resistance and antimicrobial efficacy. The composite demonstrated remarkable enhancements in the corrosion resistance of DD11 steel, notably reducing the corrosion rate from 0.34 mm/year to an impressive 0.12 mm/year. Furthermore, the material exhibited potent antimicrobial activity, especially against P. aeruginosa and C. albicans (69.23 and 84.61) as % of inhibition respectively, underscoring its immense potential for eco-friendly and sustainable applications in protective coatings. The utilization of halloysite and kojic acid, both sourced from nature, emphasizes the inherent sustainability of our approach, providing a truly green solution for surface protection with a powerful dual action: anticorrosive and antibacterial. We have thus successfully developed a novel, entirely natural-origin filler for paints offering this extraordinary dual action, all achievable through a fast and straightforward synthetic route.

1. Introduction

Research is forging ahead in creating multifunctional materials that offer a powerful one-two punch: corrosion protection and antibacterial activity. These combined features are becoming essential for things like biomedical implants and durable coatings. We're seeing exciting breakthroughs, from ZnO/CuO composites that boast enhanced antibacterial action and corrosion resistance with good biocompatibility, to Ti-Nb-N films on stainless steel that boost surface wetness, cut down bacterial sticking, and even help cells grow—making them ideal for

---

* Corresponding authors.
E-mail addresses: vincenzo.patamia@unict.it (V. Patamia), giuseppe.floresta@unict.it (G. Floresta).

[1] These authors contributed equally.

https://doi.org/10.1016/j.surfin.2025.108023
Received 23 April 2025; Received in revised form 4 September 2025; Accepted 5 November 2025

prostheses [1].

Another big leap comes with porous calcium titanate and silver nanoparticles (AgNPs) on 3D-printed titanium, which are biocompatible, fight common bacteria like Staphylococcus aureus and Escherichia coli, and show great corrosion resistance, promising a lot for bone implants [2]. For magnesium alloys, which usually corrode fast in the body, multi-layered $Nb_2O_5/Nb_2O_5-Mg/Mg$ coatings are game-changers, vastly improving their strength, wear resistance, and corrosion protection [3].

Then there are Ag-TiO_2 and Cu-Ag-TiO_2 coatings that pack a punch against viruses and microbes, all while being tough on corrosion [4]. Even graphene oxide (GO) composites are stepping up, providing both anticorrosion and antibiofilm functions, partly by creating oxidative stress that kills bacteria [5]. The polyaniline (PANI)-zirconium dioxide (ZrO_2) composite is another standout, showing synergistic antibacterial, anticorrosion, and phosphate absorption properties, even passing salt spray tests without rust [6].

Beyond coatings, Ti-Cu alloys, especially Ti-5Cu, are proving their worth for dental implants with excellent flexibility, strong antibacterial traits, and good corrosion resistance [7–9]. And clever designs like superhydrophobic basalt scales coated with AgNPs are combining reduced bacterial adhesion with a controlled release of silver ions to slow down coating breakdown and stop biofilms [10–12]. All these innovations highlight a major shift: we're increasingly designing materials "from the surface inward," meticulously controlling their chemistry and structure to achieve durable, high-performing combined properties.

The development of smart materials capable of performing multiple functions simultaneously is at the forefront of modern scientific and technological innovation. These advanced materials offer unprecedented opportunities to revolutionize industries ranging from healthcare and energy to construction and environmental monitoring [13]. By integrating versatility with adaptability, smart materials pave the way for solutions that meet complex and multifaceted challenges in real time, driving significant advancements in research and application domains [14,15].

Beyond functionality, their environmental impact has become a critical consideration. The growing need for sustainable solutions highlights the importance of designing smart materials that are high-performing and eco-friendly [16–18]. Natural resources such as clays and polysaccharides have emerged as promising candidates due to their inherent renewability, low toxicity, and compatibility with green manufacturing processes [19–21]. By leveraging such sustainable materials, researchers aim to address the dual challenge of performance and eco-consciousness, thereby contributing to a more sustainable future for materials science and its numerous applications.

Among these materials, halloysite (HNT: $Al_2Si_2O_5(OH)_4{\bullet}2H_2O$), a naturally occurring clay, stands out. Its unique tubular structure and the ease with which it can be functionalized have garnered significant attention. As a type of two-layer aluminosilicate, similar to kaolin, HNT is characterized by hollow, tube-like structures composed of alternating layers of alumina and silica [22–25]. Its applications span environmental remediation, pharmaceutical delivery systems, and catalysis [26–29], making it an ideal platform for developing multifunctional and sustainable smart materials. In particular, there has been a significant amount of recent work reported in the literature featuring HNT as a major player in the fight against bacteria and for anticorrosive applications [25,30–34]. The important properties of this material reside, in addition to its shape, mainly in its surface due to the active Si-O functional groups, which contribute both to the antibacterial activity and the electrocatalytic properties of the derivatives [35,36].

In this work, we present a truly novel multifunctional filler for protective coatings, highlighting its straightforward and rapid synthesis, as well as the exclusive use of natural-origin materials. This study aims to significantly improve and expand the functionality of a halloysite-based material by covalently functionalizing it with kojic acid and incorporating an ionic liquid. The resulting filler, due to its unique composition and ease of production, was seamlessly integrated into a protective coating that exhibits exceptional dual antibacterial and anticorrosive properties. The synergistic chelating properties of both kojic acid and the ionic liquid play a crucial role in its efficacy [37–39]. They act powerfully to inhibit iron oxidation, providing an innovative and sustainable approach to efficient surface protection. Crucially, this iron-chelating ability also actively inhibits bacterial growth by sequestering iron, an essential nutrient for bacterial proliferation. This dual mechanism of action, which is both anticorrosive and antibacterial through iron deprivation, is a key innovation.

This combination of easy synthesis, the natural origin of its components, and its dual application positions our material as a more environmentally and industrially sustainable filler compared to current alternatives. This "green" filler provides robust, multifaceted surface protection while minimizing environmental impact and promoting a circular economy within the coatings industry.

2. Materials and methods

2.1. General information

All the required chemicals were purchased from Merck and VWR. Tricationic ionic liquids (IL) were synthesized as reported in the literature (^{1}H NMR is reported in Fig. S1) [40]. Precoated aluminum sheets (silica gel 60 F254, Merck) were used for thin-layer chromatography (TLC) and visualized under UV light. ^{1}H NMR spectra were recorded at 300 K on Varian UNITY Inova using $CDCl_3$ as the solvent at 500 MHz for ^{1}H NMR. Chemical shift (δ) values were given in ppm.

2.2. Synthesis of smart materials

2.2.1. General procedure for the synthesis of HNT-K

The procedure (Scheme 1) was performed as in our previous work [26]. In a 10 mL round-bottomed reaction flask with 2 mL of DMF, 400 mg of halloysite (HNT), 1 eq., 1.36 mmol, and 1.89 mL of triethylamine (Et_3N) were added. The mixture was then agitated for 30 min at room temperature. Chlorokojic acid (K) (1.30 g, 6 eq, 8.16 mmol) was added, and the reaction mixture was stirred overnight at 80 °C. After filtering the precipitate, it was thoroughly cleaned with acetone (5 × 10 mL) and dried in an oven set at 65 °C overnight, yielding 1.58 g of pure product.

2.2.2. Loading of IL in HNT-K

10 mg of tricationic ionic liquids (IL) was dissolved in 1 mL of water, and 100 mg of HNT-K was added. The resulting mixture was sonicated for 30 min and shaken overnight at room temperature. After agitation, the mixture was centrifuged, and the supernatant was removed. The remaining solid was dried under vacuum to obtain HNT-K-IL (Scheme 1).

2.2.3. General procedure for loading of filler (HNT-K-IL) in paint

HNT-K-IL filler was incorporated into a commercial white water-based paint (Natural Pigments, Inc., ZnO as pigment, Gum Arabic as binder) using a 3 % wt and 9 % wt formulation for anti-corrosion testing and a 9 % wt formulation for antibacterial testing. Specifically, HNT-K-IL filler was added to the water-based paint in the ratios 3 % wt and 9 % wt, and they were mixed with a glass rod until a homogeneous system was formed. Then to carry out the anti-corrosion tests, the paint was spread on a substrate of DD11 steel foil (HarrisSteels, Ltd., of 20 × 20 mm and 1.5 mm thickness with the following composition % wt: C 0.12, Mn 0.6, P 0.045, S 0.045, Fe balance), forming a homogeneous layer of paint covering an entire face of the substrate above by adding a small amount of water to facilitate the coating. Then the paint was left to air dry for 48 h before undergoing to anti-corrosion studies.

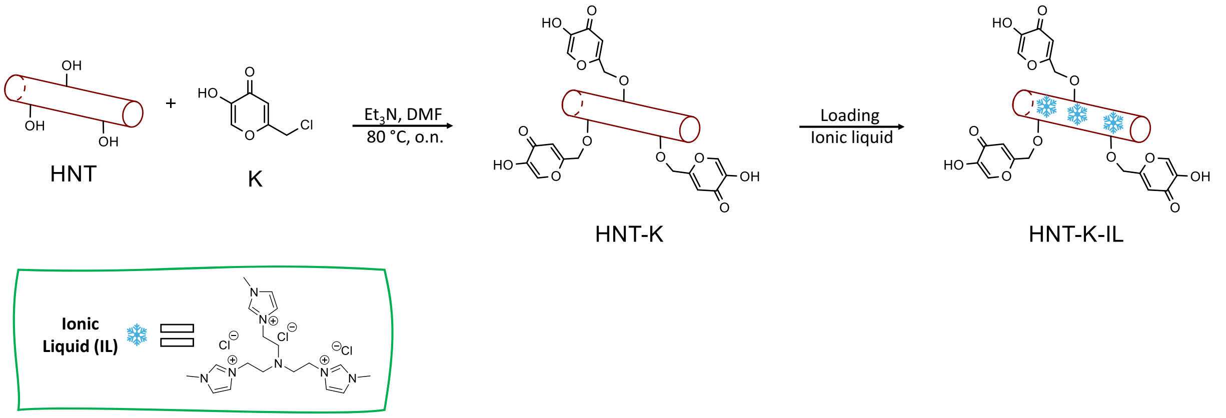

Scheme 1. Preparation of filler HNT-K-IL.

2.3. Experimental setup

2.3.1. General procedure for antibacterial and antifungal test

The antibacterial and antifungal activity of paint formulations was tested against four bacterial strains (S. aureus, S. marcescens, P. aeruginosa, and E. coli) and the fungal strain C. albicans. Bacterial suspensions were prepared to a 0.5 McFarland standard (OD 0.180–0.200 for bacteria, OD ~0.150 for fungi), corresponding to approximately 1.5×10^8 CFU/mL. Two serial dilutions (1:10) were performed to achieve a final 10^{-6} CFU/mL concentration. For each strain, 1 mL of the diluted suspension was inoculated into sterile test tubes with white caps.

Nitrocellulose filter paper squares (6 mm × 6 mm) were prepared in triplicate for each condition. 400 mg of each paint formulation were mixed with 600 μL of sterile water to create liquid formulations. The filter paper squares were impregnated with the paint solutions, dried at room temperature for >24 h under sterile conditions, and added to the test tubes containing bacterial or fungal suspensions.

Sterile test tubes were prepared as follows: 15 tubes for base paint, 15 for paint with filler, 15 for positive controls, and 6 for negative controls (3 in Mueller-Hinton broth for bacteria and 3 in RPMI medium without red phenol for fungi). For the positive control, tubes were treated with a standard antibacterial or antifungal agent. On the experimental day, additional red-capped tubes were prepared for each strain, using Mueller-Hinton broth (for bacteria) or RPMI medium (for fungi). Each test condition was performed in triplicate. Serial dilutions of the bacterial and fungal suspensions were prepared, and 100 μL of each dilution were plated on pre-warmed agar plates: Plate Count Agar (PCA) for bacterial strains and Sabouraud Dextrose Agar (SAB) for fungal strains. Plates were incubated overnight at 37 °C for bacteria and 33 °C for fungi. The following day, colonies were counted from the plates to assess bacterial and fungal growth inhibition. This setup allowed the evaluation of the antimicrobial efficacy of the base paint and the paint with filler compared to controls.

2.3.2. General procedure for anticorrosion test

Electrochemical tests were performed by immersing the DD11 steel foil in a NaCl 3 % wt water solution. A screen-printed carbon electrode (SPCE), consisting of a carbon working electrode, a carbon auxiliary electrode, and an Ag/AgCl reference electrode, was used for the present measurements performed in air. Cycle Voltammetry (CV), Open Circuit Potentiometry (OCP), and Linear Polarization Resistance (LPR) measurements were performed with a DropSens μStat 400 potentiostat using the Dropview 8400 software. CV tests were performed at a scan rate of 50 mV/s in the −0.4–1.0 V potential range. A 1.0 mM potassium ferricyanide standard stock solution ($K_3[Fe(CN)_6]$) was used to get a calibration curve. OCP tests were conducted by monitoring the potential change over time for 250 s. LPR tests were performed using a 0.001 V potential step (E_{step}), a 5 s preconditioning time ($t_{precond}$), and a scan rate of 1 mV/s in the −0.3–0.3 V potential range. The LPR Tafel parameters (R_p^0 = polarization resistance of DD11; R_p = polarization resistance of DD1-HNT-K-IL; I_{corr} = current at the intersection of cathodic and anodic Tafel lines; J_{corr} = corrosion density current; beta$_a$ = anodic slope; beta$_c$ = cathodic slope; corr. rate = corrosion rate) were evaluated using the extrapolation method [41]. Each test was performed in triplicate.

2.4. Characterization

2.4.1. Infrared spectroscopy

FTIR-ATR analyses were conducted using an FTIR Agilent Cary 630 equipped with an ATR sampling module. Thin films of all samples were placed on the ATR crystal and pressed. The results were derived from 16 scans acquired in the 4000–500 cm^{-1} range with a resolution of 2 cm^{-1} at room temperature.

2.4.2. Thermogravimetric analysis

TGA analysis was performed with a TGA TA instrument Q500 according to the following method: heating under a nitrogen blanket from 30 °C to 300 °C at 10 °C/min, isothermal step at 300 °C for 15 min, heating to 550 °C at 20 °C/min, isothermal step for 15 min, heating to 900 °C at 10 °C/min, isothermal step for 3 min, shift from nitrogen to air, final isothermal step for 30 min.

2.4.3. Transmission electron microscopy coupled with energy-dispersive X-ray spectroscopy

Transmission electron microscopy (TEM) was done using a probe-corrected JEOL JEM ARM 200F equipped with a cold field emission gun (C-FEG) and a Centurio large-angle silicon drift detector (SSD) for energy dispersive X-ray spectroscopy (EDS). Images were acquired in scanning mode (STEM) at 200 kV acceleration voltage.

HNT-K-IL was dispersed and ultrasonicated in ethyl acetate and then drop-cast on a copper TEM grid with a lacey film supporting an ultrathin film (<3 nm) of amorphous carbon [26,42].

2.4.4. X-ray photoelectron spectra (XPS)

X-ray photoelectron spectra (XPS) were measured at a 45° take-off angle relative to the surface sample holder with a PHI 5000 Versa Probe II system (ULVAC-PHI, INC., base pressure of the main chamber 1×10^{-8} Pa) [43,44]. Samples were excited with the monochromatized Al Kα X-ray radiation using a pass energy of 5.85 eV. The instrumental energy resolution was ≤0.5 eV. The XPS peak intensities were obtained after Shirley's background removal [43,44]. Spectra calibration was achieved by fixing the Ag $3d_{5/2}$ peak of a clean sample at 368.3 eV [45,46]. The atomic concentration analysis was performed by considering the relevant atomic sensitivity factors. Some XP spectra were fitted using the XPSPEAK4.1 software by fitting the spectral profiles with Gaussian envelopes after subtraction of the background. This process involves data refinement using the least squares fitting method until the highest possible correlation between the experimental spectrum and the theoretical profile is achieved. The residual or agreement factor R, defined by $R = [\Sigma(F_{obs} - F_{calc})^2/\Sigma(F_{obs})^2]^{1/2}$, after minimization of the function $\Sigma(F_{obs} - F_{calc})^2$, converged to the value of 0.03.

2.4.5. Evaluation of mean particle size, polydispersity index, and zeta potential

To evaluate the mean particle size (Z-ave), polydispersity index (PdI), and Zeta potential (ZP) of HNT, HNT-K, IL, and HNT-K-IL, they were solubilized/suspended in water (1 mg/mL) and analyzed using Photon Correlation Spectroscopy (PCS) with a Zetasizer Nano S90 instrument (Malvern Instruments, Malvern, UK). The instrument was set with a detection angle of 90 °C and a 4 mW He-Ne laser operating at 633 nm, at a temperature of 25 °C. Three sets of measurements were used in the sample analysis, and the mean size ± standard deviation (SD) was the reported result. The Smoluchowski equation, which incorporates the average values of particle mobility and has a constant of 1.5, was utilized by the software to calculate the ZP values. The mean of three sets of up to 100 measurements is used to report ZP values.

3. Results and discussion

3.1. Synthesis

The HNT-based filler was synthesized following a recently reported method [26], exploiting the hydroxyl groups on the HNT surface for covalent functionalization with chlorokojic acid (K), a kojic acid derivative known for its chelating properties [28] (Scheme 1). Subsequently, an ionic liquid (IL), synthesized according to literature protocols [40], was loaded onto the surface of the nanocontainer.

The IL, featuring three imidazole groups, enhances interaction with iron [17], working synergistically with the naturally derived chelating agent K to efficiently chelate iron. This dual action imparts the natural nanofiller with antibacterial and anticorrosive properties, reinforcing its potential for protective applications.

3.2. Characterizations

The degree of functionalization (%f) was determined by thermogravimetric analysis (thermogram is shown in Fig. S2), following the method reported in our previous work [26], yielding a %f of 53 % for HNT-K. In particular, we note three most significant temperature ranges: at T < 150 °C, where the loss of free interlayer water occurs [47]; 150 °C < T < 550 °C, where the degradation of the organic component, i.e. K, occurs, thanks to which we calculate the degree of functionalization [26, 48]; and finally at T > 550 °C, dehydroxylation occurs (condensation of the hydroxyl groups of the inner aluminum sheets), and SO_2 is released due to the thermal decomposition of sulfides (as impurities) or alunite, as recently reported in the literature [49]. FTIR analysis was conducted to confirm the presence of IL and the functionalization of HNT-K. Fig. 1 presents the FTIR spectra of IL (red line) and HNT-K-IL (black line). In addition to the typical bands of HNT-K previously reported [26,28] and shown in the figure, two distinct bands at 840 and 1170 cm^{-1}, corresponding to vibrational modes and C—N stretching, respectively, were observed [50,51]. These features, highlighted by dashed lines in Fig. 1 (black spectrum), confirm the successful presence of IL onto the HNT-K surface.

The particle size and surface charge of HNT, HNT-K, IL, and HNT-K-IL solutions/suspensions were analyzed using PCS (Table 1). The results confirmed that HNT exhibited a size in the micrometer range (1328 nm), consistent with literature reports [52]. Additionally, the nanotubes carried a negative surface charge (−37.8 mV) due to deprotonated silanol groups, which are crucial in ensuring good colloidal stability by preventing aggregation and promoting dispersion in solution [52,53]. Functionalization with K led to an increase in size (2446 nm), a decrease in polydispersity (from 0.623 to 0.470), and a slight shift to a positive charge (9.7 mV), suggesting that functionalization with K neutralizes the negative charges of the HNT by binding most of the hydroxyl groups on its outer surface [54,55]. Loading IL onto HNT-K resulted in a significant increase in ZP (41.7 mV), confirming the successful presence of IL onto the HNT-K surface with typical electrostatic interactions [55,56]. Furthermore, HNT-K-IL exhibited a notable size reduction (453.4 nm), likely due to the enhanced solubility of HNT-K in aqueous solution facilitated by IL [57]. This is further supported by the low PdI (PdI <0.5), indicating the improved particle uniformity and homogeneity [58]. Particle size and PDI are considered indirect indicators of a compound's solubility and colloidal stability: smaller particle sizes and lower PDI values are typically associated with better solubility and reduced aggregation [59]. In our case, the observed improvements suggest that the presence of IL increased the aqueous solubility of HNT-K. This hypothesis is consistent with findings reported by Domínguez-Delgado et al [59], who demonstrated that the use of more polar solvents led to nanoparticles with reduced size and PDI, directly correlating with improved polymer solubility. Therefore, the enhanced solubility of HNT-K in our system may be attributed to a similar mechanism driven by the polar nature of the IL.

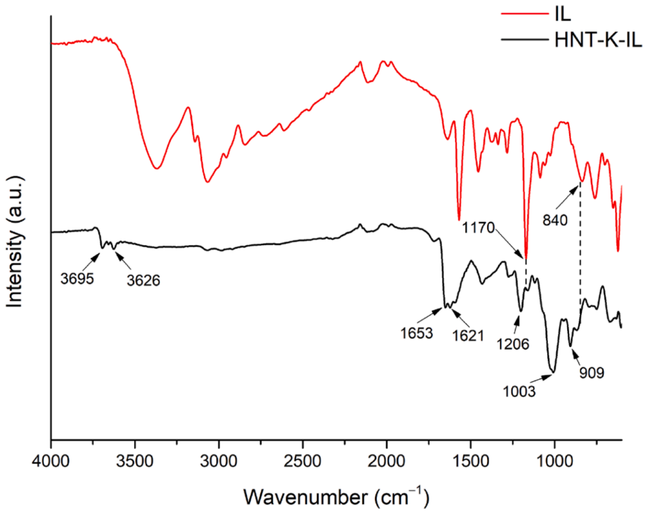

Fig. 1. Stacked FT-IR spectra of IL (red line) and HNT-K-IL (black line).

Table 1
Mean size (Z-ave), polydispersity index (PdI), and zeta potential (ZP) of HNT, HNT-K, IL, and HNT-K-IL.

Sample	Z-ave (nm) ±SD	PDI ±SD	ZP ±SD (mV)
HNT	1328 ± 215.3	0.623 ± 0.14	−37.8 ± 1.50
HNT-K	2446 ± 345.0	0.470 ± 0.14	9.7 ± 0.24
IL	1568 ± 140.1	0.902±0.17	17.6 ± 1.77
HNT-K-IL	453.4 ± 7.5	0.276 ± 0.11	41.7 ± 0.36

The XPS survey spectra of HNT-K and HNT-K-IL (Fig. S3) reveal the presence of Al, Si, and O, consistent with the halloysite composition and some adventitious carbon in the HNT-K. K and IL within the nanotubes contributed additional signals (Fig. S4). In the HNT-K-IL sample, additional peaks were observed at 401.7 and 198.7 eV, corresponding to the N 1 s and Cl 2p levels, respectively, confirming the successful surface functionalization of HNT-K with the ionic liquid (Fig. 2). Deconvolution of the 401.7 eV N 1 s peak using two Gaussian components revealed contributions at 400.6 eV (attributed to the four tertiary nitrogen atoms in the IL structure, 55 % relative intensity) and 402.2 eV (corresponding to the three quaternary nitrogen atoms, 45 % relative intensity). These values align well with the expected electronic environment of the IL, further supporting its presence. Experimental atomic concentration

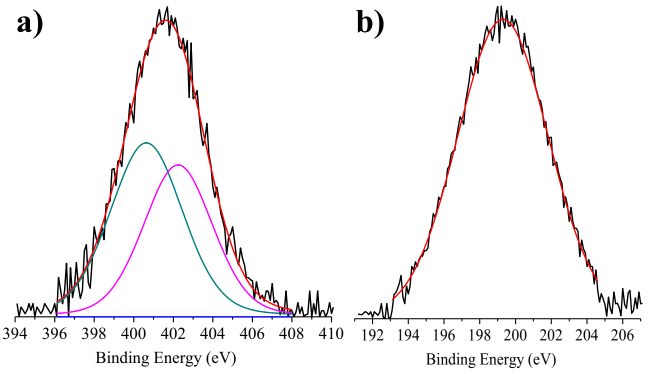

Fig. 2. Al Kα-excited XPS spectra of the HNT-K-IL samples in the: a) N 1 s binding energy region: dark cyan and magenta lines refer to the 400.6 and 402.2 eV Gaussians components, respectively, the blue line represents the background, and the red line superimposed on the experimental black profile refers to the sum of the Gaussian components; b) Cl 2p binding energy region.

analysis confirmed the presence of 1.7 % nitrogen in the HNT-K-IL sample, consistent with the nominal composition of the ionic liquid.

Fig. 3 shows a STEM image of the HNT-K-IL composite, acquired using a medium-angle annular dark field (MAADF) detector, which allowed us to visualize the nanotube morphology. The observed nanotubes exhibit their characteristic dimensions of approximately 500 × 100 nm (length × diameter) [26].

EDS and TEM analyses confirm the composite composition, consistent with the XPS findings (Figs. S5 and S6).

3.3. Antibacterial activity

The antimicrobial efficacy of the two paint formulations, base paint and paint with filler (HNT-K-IL), was assessed against four bacterial strains (S. aureus, P. aeruginosa, S. marcescens, and E. coli) and one fungal strain (C. albicans). The results, summarized in Table 2, show varying degrees of inhibition across different microorganisms. Base Paint: the base formulation showed moderate antimicrobial activity, with percentage inhibition ranging from 15.87 % (S. aureus) to 62.30 % (C. albicans). The activity was notably weaker against bacterial strains compared to the fungal strain.

Paint with filler (HNT-K-IL, 9 % wt): incorporating the HNT-K-IL significantly enhanced the antimicrobial efficacy of the paint. The percentage inhibition was markedly higher for all microorganisms, ranging from 47.36 % (E. coli) to 84.61 % (C. albicans). The filler addition substantially improved, particularly against P. aeruginosa (69.23 %) and C. albicans. Overall, the paint with filler consistently outperformed the base paint across all tested strains, indicating its superior antimicrobial properties. These findings highlight the potential of incorporating fillers to enhance the functional properties of paint formulations for inhibiting microbial growth. In addition, the presence of IL on HNT-K enables a synergistic effect, broadening the spectrum of biocidal action, which represents a notable improvement compared to previously reported formulations [28].

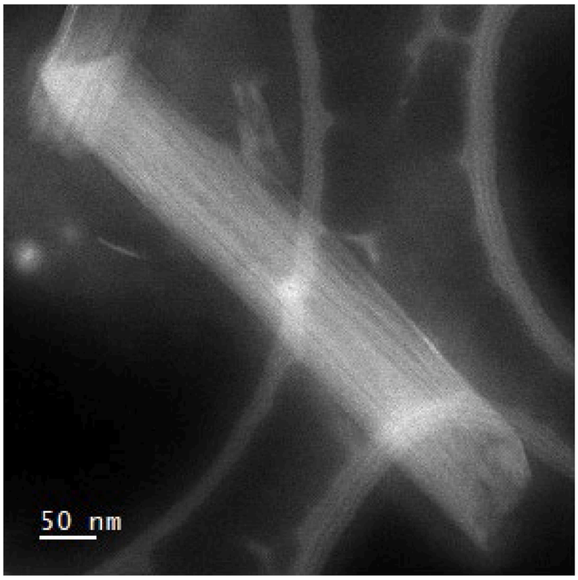

Fig. 3. MAADF STEM image of HNT-K-IL.

Table 2
Percentage inhibition of microbial growth for paint formulations.

Sample	S. aureus	P. aeruginosa	S. marcescens	E. coli	C. albicans
Base Paint	15.87	30.76	46.15	21.05	62.30
Paint with HNT-K-IL	63.49	69.23	61.53	47.36	84.61

3.4. Anticorrosion test

To assess the ability of our HNT-based paint to prevent iron ions leakage, we performed CV measurements after immersing DD11 steel foils in a 3 % wt NaCl solution. The measurements were performed shortly after immersion, as described in previous studies [60]. Fig. 4a shows the CV profiles of DD11 steel foil, DD11 cover with paint (DD11-P), DD11 cover with paint incorporating the HNT-K filler (DD11-P-HNT-K), DD11 cover with paint incorporating 3 % wt and 9 % wt of HNT-K-IL, respectively (DD11-P-HNT-K-IL3 and DD11-P-HNT-K-IL9). The anodic peak (0.18 V) corresponding to the oxidation of $Fe^{2+/3+}$ and the cathodic peak (0.04 V), related to the reduction of $Fe^{3+/2+}$, clearly indicate iron leakage in the NaCl solution (Fig. 4b). The iron leakage decreases in the sequence of DD11 steel foil, DD11-P, DD11-P-HNT-K, DD11-P-HNT-K-IL3 and DD11-P-HNT-K-IL9, suggesting that the filler effectively inhibits it.

Furthermore, using a calibration curve derived from a standard solution of $K_3[Fe(CN)_6]$, we were able to calculate the released amount of Fe ions (Fig. 5). By analyzing the anodic oxidation peaks (Ipa) for DD11 steel foil, DD11-P, DD11-P-HNT-K, DD11-P-HNT-K-IL3, and DD11-P-HNT-K-IL9, the corresponding iron concentrations were found to be 70, 65, 50, 20 and 17 μmol/L ions, respectively. These results demonstrate a >70 % reduction in the iron release in solution for the HNT-K-IL-treated samples, indicating the filler's effectiveness in inhibiting the corrosion process.

The Tafel curves, obtained by the LPR analyses of the same solutions, allowed for the calculation of polarization resistance (R_P) values: 316, 221, 726, 1701, and 665 kΩ for DD11, DD11-P, DD11-P-HNT-K, DD11-P-HNT-K-IL3, and DD11-P-HNT-K-IL9, respectively. It is known that an increase in metal resistance corresponds to a decreased corrosion tendency (rusting) [60]. The highest R_p value was observed for the DD11-P-HNT-K-IL3 sample. Based on the R_P data from the Tafel curves, we calculated the corrosion inhibition efficiency (%)η_{EIS}, using Eq. (1) [45], resulting in 81.4 %.

$$(\%)\eta_{EIS} = \left(1 - \frac{R_P^0}{R_P}\right) \times 100 \tag{1}$$

Next, each sample was immersed in a 3 % wt NaCl solution for 24 h to simulate the corrosion process [61]. After this period, we performed OCP and LPR measurements over time. The OCP curves of DD11, DD11-P, DD11-P-HNT-K, and DD11-P-HNT-K-IL3 (Fig. 6a) shifted towards lower potentials. This behavior suggests that the HNT-KIL molecule affects the cathodic reactions and acts as a cathodic inhibitor. The constant OCP trend observed after 24 h of immersion for DD11 and

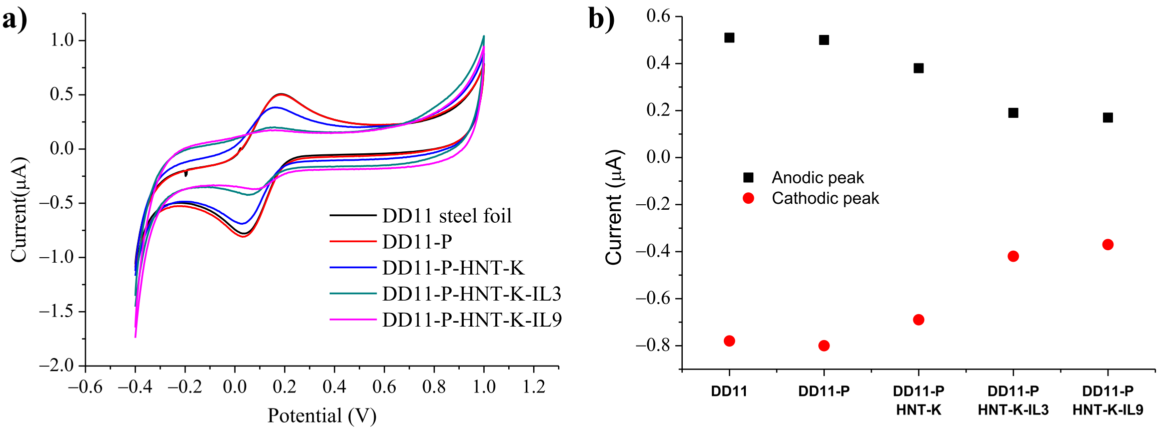

Fig. 4. a) Cyclic voltammograms of DD11 steel foil, DD11-P, DD11-P-HNT-K, DD11-P-HNT-K-IL3, and DD11-P-HNT-K-IL9 immersed in a NaCl (3 %) aqueous solution, measured with an SPCE at 50 mV/s scan rate, 25 °C; b) Anodic and cathodic peaks of DD11-P, DD11-P-HNT-K, DD11-P-HNT-K-IL3, and DD11-P-HNT-K-IL9.

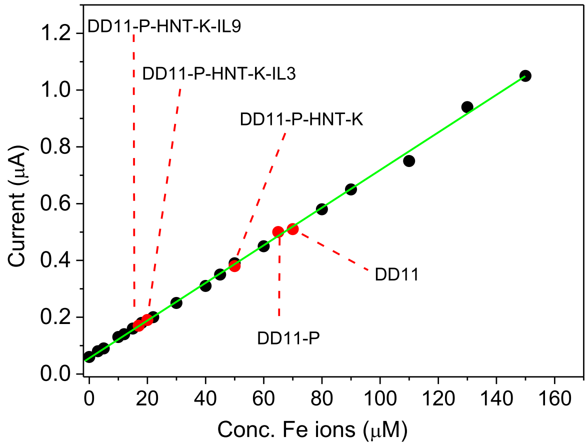

Fig. 5. Quantification of Fe^{2+} released from samples in a NaCl solution (3 % wt) after 10 s immersion; Black dots refer to the current measured for different ($K_3[Fe(CN)_6]$) concentrations. Red dots refer to the current measured with the SPCE for NaCl (3 % wt) water solutions containing DD11 steel foil, DD11-P, DD11-P-HNT-K, DD11-P-HNT-K-IL3, and DD11-P-HNT-K-IL9, respectively. The green calibration line superimposed on the experimental dots refers to the fitting.

DD11-P-HNT-K-IL3 implies that no further material dissolution occurred in the solutions [62,63].

Inspection of Fig. 6b, which shows the LPR data for DD11 and DD11-P-HNT-K-IL3, reveals a 60 mV decrease in E_{corr} for DD11-P-HNT-K-IL3 compared to DD11. The shift of E_{corr} to negative potentials indicates that DD11-P-HNT-K-IL3 primarily acts at the cathode. The values extrapolated from the Tafel curves, presented in Table 3, show a decrease in the corrosion density current (j_{corr}) from DD11 to DD11-P-HNT-K-IL3, indicating a reduction in the corrosion phenomenon in the presence of HNT-K-IL3. The corrosion rate of DD11-P-HNT-K-IL3 (0.12 mm/year) is significantly lower than that of DD11 (0.34 mm/year) [64,65], indicating a substantial improvement in corrosion resistance.

4. Conclusions

This study demonstrates the potential of halloysite nanotube (HNT)-based composites functionalized with kojic acid and loaded with an

Table 3
Polarization parameters for DD11 and DD11-P-HNT-K-IL3 corrosion.

Samples	I_{corr} (mA)	J_{corr} (mA/cm^2)	ba (mV/dec)	bc (mV/dec)	Corr. rate (mm/year)
DD11	3.65	29.20	180	390	0.34
DD11-P-HNT-K-IL3	1.30	10.40	40	150	0.12

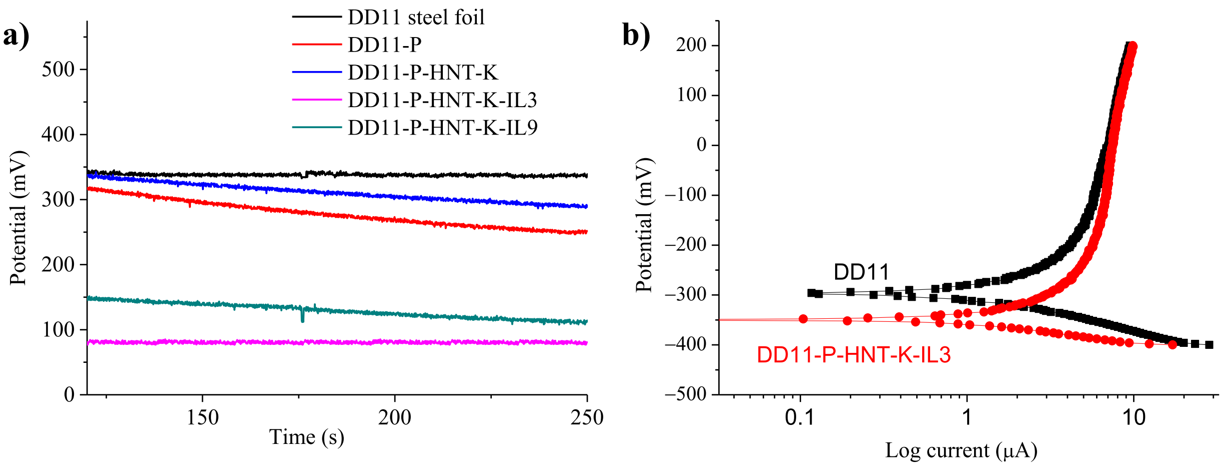

Fig. 6. a) OCP versus time curves in NaCl solution (3 % wt) for DD11 steel foil, DD11-P, DD11-P-HNT-K, DD11-P-HNT-K-IL3, and DD11-P-HNT-K-IL9; b) Polarization curves of DD11 steel foil and DD11-P-HNT-K-IL3.

ionic liquid as a multifunctional additive for sustainable protective coatings. The composite material effectively combines antibacterial and anticorrosive properties, making it a promising candidate for various industrial applications that require enhanced surface protection, such as the automotive, marine, and construction sectors. The dual functionality is achieved through the synergistic interaction between the naturally derived components: kojic acid, which provides chelating properties to inhibit iron oxidation, and the ionic liquid, which enhances the material's stability and resistance to corrosion.

The study confirmed that the HNT-K-IL composite offers superior protection compared to conventional coatings, with significant reductions in the corrosion rate of DD11 steel from 0.34 mm/year to 0.12 mm/year, highlighting its effectiveness as an anticorrosive agent. The results also show that the composite possesses enhanced antimicrobial activity, particularly against P. aeruginosa and C. albicans, further expanding its utility in preventing microbial growth on coated surfaces. The synergistic effect between the ionic liquid and the chelating agent is crucial in providing broad-spectrum activity, which outperforms previously reported materials in terms of antimicrobial efficacy.

Furthermore, the use of halloysite and kojic acid, both naturally sourced materials, emphasizes the sustainability of the developed composite. This eco-friendly approach aligns with the growing need for greener and more sustainable alternatives to conventional synthetic coatings that often involve harmful chemicals and have a higher environmental impact. By leveraging the unique properties of natural clays and biomolecules, this work contributes to the development of sustainable materials that do not compromise performance.

Looking ahead, there is significant potential to optimize the scalability of this composite material for large-scale applications while maintaining its functional efficacy and sustainability. Future research efforts could explore applying this approach to a broader range of substrates and operational environments, including those in extreme weather conditions or highly corrosive environments. Additionally, expanding the range of microbial strains tested will provide deeper insights into the antimicrobial spectrum of the composite, potentially improving its effectiveness against a wider array of pathogens.

Ultimately, this study positions HNT-K-IL composites as a versatile, green, and cost-effective solution for surface protection—an essential step towards advancing the field of innovative materials with a focus on sustainability, multifunctionality, and environmental compatibility. Through continued research and development, these materials could play a pivotal role in addressing global challenges related to corrosion prevention, microbial contamination, and eco-friendly technologies.

CRediT authorship contribution statement

Erika Saccullo: Visualization, Validation, Methodology, Investigation. **Angelo Ferlazzo:** Writing – original draft, Validation, Methodology, Investigation. **Virginia Fuochi:** Writing – original draft, Methodology, Investigation. **Salvatore Furnari:** Validation, Methodology, Investigation. **Rosamaria Lombardo:** Writing – original draft, Validation, Methodology, Investigation. **Luca Spitaleri:** Writing – original draft, Validation, Methodology, Investigation. **Gianfranco Sfuncia:** Writing – original draft, Methodology, Investigation. **Giuseppe Nicotra:** Supervision, Methodology, Investigation. **Pio Maria Furneri:** Writing – review & editing, Resources. **Antonino Gulino:** Writing – review & editing, Supervision, Resources, Formal analysis. **Rosario Pignatello:** Writing – review & editing, Supervision, Resources, Formal analysis. **Antonio Rescifina:** Writing – review & editing, Resources, Project administration, Funding acquisition. **Vincenzo Patamia:** Writing – review & editing, Writing – original draft, Visualization, Supervision, Project administration, Formal analysis, Conceptualization. **Giuseppe Floresta:** Writing – review & editing, Supervision, Resources, Project administration, Conceptualization.

Declaration of competing interest

The authors declare that they have no known competing financial interests or personal relationships that could have appeared to influence the work reported in this paper.

Acknowledgements

The research leading to these results has received funding from the European Union—NextGenerationEU through the Italian Ministry of University and Research under PNRR—M4C2-I1.3 Project PE_00000019 "HEAL ITALIA" (Antonio Rescifina, Vincenzo Patamia, and Erika Saccullo), CUP E63C22002080006.

The views and opinions expressed are those of the authors only and do not necessarily reflect those of the European Union or the European Commission. Neither the European Union nor the European Commission can be held responsible for them. This research was supported by EU funding within the NextGeneration EU-MUR PNRR Extended Partnership on Emerging Infectious Diseases Project N. PE00000007 "INF-ACT" (Pio Maria Furneri and Salvatore Furnari). The authors Angelo Ferlazzo and Antonino Gulino thank the European Union (NextGeneration EU) through the MUR-PNRR project SAMOTHRACE (ECS00000022) for funding.

Supplementary materials

Supplementary material associated with this article can be found, in the online version, at doi:10.1016/j.surfin.2025.108023.

Data availability

Data will be made available on request.

References

[1] G. Zhang, J. Liu, Y. Zhu, T. Shen, D.q. Yang, Enhanced antibacterial efficacies, corrosion resistance, and cytocompatibility of ZnO/CuO composite coatings through designed sputtering orders, Appl. Surf. Sci. 635 (2023) 157724.

[2] A. Rodriguez-Contreras, D. Torres, B. Rafik, M. Ortiz-Hernandez, M.P. Ginebra, J. A. Calero, J.M. Manero, E. Ruperez, Bioactivity and antibacterial properties of calcium-and silver-doped coatings on 3D printed titanium scaffolds, Surf. Coat. Technol. 421 (2021) 127476.

[3] M. Ferreira, K. dos Santos, D. Bon, R. Gelamo, R. Galo, N. Leite, C. Baptista, H. C. Pinto, J. Moreto, The positive impact of the reactive sputtered nanostructured Nb2O5 coatings to reduce the FCG rates of the 2524-T3 alloy in an aggressive medium, Emergent. Mater. 7 (5) (2024) 2129–2141.

[4] M. Birkett, L. Dover, C. Cherian Lukose, A.Wasy Zia, M.M. Tambuwala, Á. Serrano-Aroca, Recent advances in metal-based antimicrobial coatings for high-touch surfaces, Int. J. Mol. Sci. 23 (3) (2022) 1162.

[5] Y. Zhou, H. Wang, C. Zhang, Q. Zhou, D.F. Rodrigues, Graphene oxide-hybridized waterborne epoxy coating for simultaneous anticorrosive and antibiofilm functions, Front. Mater. Volume 9 (2022), 2022.

[6] F.C.P. Masim, C.H. Tsai, Y.F. Lin, M.L. Fu, M. Liu, F. Kang, Y.F. Wang, Synergistic effect of PANI–ZrO2 composite as antibacterial, anti-corrosion, and phosphate adsorbent material: synthesis, characterization and applications, Env. Technol. 40 (2) (2019) 226–238.

[7] E. Zhang, X. Wang, M. Chen, B. Hou, Effect of the existing form of Cu element on the mechanical properties, bio-corrosion and antibacterial properties of Ti-Cu alloys for biomedical application, Mater. Sci. Eng. 69 (2016) 1210–1221.

[8] X. Zhao, J. Hu, J. Nie, D. Chen, G. Qin, E. Zhang, Enhanced antibacterial activity, corrosion resistance and endothelialization potential of Ti-5Cu alloy by oxygen and nitrogen plasma-based surface modification, J. Mater. Sci. Technol. 168 (2024) 250–264.

[9] M.R. Akbarpour, H.M. Mirabad, A. Hemmati, H.S. Kim, Processing and microstructure of Ti-Cu binary alloys: a comprehensive review, Prog. Mater. Sci. 127 (2022) 100933.

[10] Z. Li, L. Liu, H. Zheng, F. Meng, F. Wang, Superhydrophobic, corrosion resistance, and antibacterial coating with delayed release of Ag ions, Compos. Commun. 31 (2022) 101134.

[11] H. Zheng, L. Liu, F. Meng, Y. Cui, Z. Li, E.E. Oguzie, F. Wang, Multifunctional superhydrophobic coatings fabricated from basalt scales on a fluorocarbon coating base, J. Mater. Sci. Technol. 84 (2021) 86–96.

[12] Z. Li, L. Liu, H. Zheng, F. Meng, F. Wang, Thermoresponsive PNIPAm on anti-corrosion antibacterial coating for controlled Ag ions release, Compos. Commun. 35 (2022) 101327.

[13] S. Bahl, H. Nagar, I. Singh, S. Sehgal, Smart materials types, properties and applications: a review, Mater. Today 28 (2020) 1302–1306.

[14] R. Seif, F.Z. Salem, N.K. Allam, E-waste recycled materials as efficient catalysts for renewable energy technologies and better environmental sustainability, Environ. Dev. Sustain. 26 (3) (2024) 5473–5508.

[15] N. Singh, F. Colangelo, I. Farina, Green Materials: Sustainable Materials, Green Nanomaterials, Concepts in Smart Societies, CRC Press, 2024, pp. 43–71.

[16] R. Sharma, P.C. Nath, Y.K. Mohanta, B. Bhunia, B. Mishra, M. Sharma, S. Suri, M. Bhaswant, P.K. Nayak, K. Sridhar, Recent advances in cellulose-based sustainable materials for wastewater treatment: an overview, Int. J. Biol. Macromol. 256 (2024) 128517.

[17] G. Choudhary, J. Dhariwal, M. Saha, S. Trivedi, M.K. Banjare, R. Kanaoujiya, K. Behera, Ionic liquids: environmentally sustainable materials for energy conversion and storage applications, Environ. Sci. Pollut. Res. 31 (7) (2024) 10296–10316.

[18] E. Saccullo, V. Patamia, C. Zagni, A. Rescifina, G. Floresta, Learning strategies from Nature's blueprint to cyclic carbonate synthesis, ChemSusChem. e202402061.

[19] M. Fahimizadeh, L.W. Wong, Z. Baifa, S. Sadjadi, S.A.B. Auckloo, K. Palaniandy, P. Pasbakhsh, J.B.L. Tan, R.R. Singh, P. Yuan, Halloysite clay nanotubes: innovative applications by smart systems, Appl. Clay. Sci. 251 (2024) 107319.

[20] V. Patamia, E. Saccullo, F. Magaletti, V. Fuochi, S. Furnari, R. Fiorenza, P. M. Furneri, V. Barbera, G. Floresta, A. Rescifina, Nature-inspired innovation: alginic-kojic acid material for sustainable antibacterial and carbon dioxide fixation, Int. J. Biol. Macromol. 277 (2024) 134514.

[21] V. Patamia, E. Saccullo, V. Fuochi, F. Magaletti, L. Trecarichi, S. Furnari, P. M. Furneri, V. Barbera, G. Floresta, A. Rescifina, Developing advanced antibacterial alginic acid biomaterials through dual functionalization, ACS. Appl. Bio Mater. (2024).

[22] M. Massaro, R. Noto, S. Riela, Halloysite nanotubes: smart nanomaterials in catalysis, Catalysts 12 (2) (2022) 149.

[23] E.S. Goda, K.R. Yoon, S.H. El-sayed, S.E. Hong, Halloysite nanotubes as smart flame retardant and economic reinforcing materials: a review, Thermochim. Acta 669 (2018) 173–184.

[24] K.A. Zahidah, S. Kakooei, M.C. Ismail, P.B. Raja, Halloysite nanotubes as nanocontainer for smart coating application: a review, Prog. Org. Coat. 111 (2017) 175–185.

[25] M. Topuz, Y. Akinay, E. Karatas, T. Cetin, Ti3C2Tx MXene-functionalized hydroxyapatite/halloysite nanotube filled poly– (lactic acid) coatings on magnesium: in vitro and antibacterial applications, J. Magnes. Alloys 12 (9) (2024) 3758–3771.

[26] E. Saccullo, V. Patamia, F. Magaletti, G. Dativo, M. Camarda, R. Fiorenza, V. Barbera, G. Floresta, A. Rescifina, Halloysite-kojic acid conjugate: a sustainable material for the photocatalytic CO2 reduction and fixation for cyclic carbonates production, J. CO2. Util. 85 (2024) 102865.

[27] C. Zagni, A.A. Scamporrino, P.M. Riccobene, G. Floresta, V. Patamia, A. Rescifina, S.C. Carroccio, Portable nanocomposite system for wound healing in space, Nanomaterials 13 (4) (2023) 741.

[28] V. Patamia, C. Zagni, R. Fiorenza, V. Fuochi, S. Dattilo, P.M. Riccobene, P. M. Furneri, G. Floresta, A. Rescifina, Total bio-based material for drug delivery and iron chelation to fight cancer through antimicrobial activity, Nanomaterials 13 (14) (2023) 2036.

[29] E. Saccullo, G. Dativo, R. Lombardo, M.T.A. Iapichino, R. Fiorenza, V. Patamia, G. Floresta, Natural antenna molecule in halloysite-kojic acid composite for the solar photocatalytic CO2 methanation, Mater. Today Chem. 44 (2025) 102587.

[30] S. Kiani, V. Haddadi-Asl, A. Khosravi, H.E. Mohammadloo, H. Ahmadi, Designing a smart polyurethane anti-corrosion coating loaded with APTES/IMZ modified halloysite nanotubes, Surf. Coat. Technol. 492 (2024) 131179.

[31] X. Shan, Z. Zou, Z. Mi, K. Tong, C. Hou, Preparation of smart self-healing coatings on zinc surfaces using halloysite nanotubes loaded with corrosion inhibitors, Langmuir. 40 (47) (2024) 25236–25249.

[32] Y. Liu, J. Shi, Design of a smart protective coating with molybdate-loaded halloysite nanotubes towards corrosion protection in reinforced concrete, Cem. Concr. Compos. 147 (2024) 105419.

[33] M. Chozhanathmisra, N. Murugan, P. Karthikeyan, S. Sathishkumar, G. Anbarasu, R. Rajavel, Development of antibacterial activity and corrosion resistance properties of electrodeposition of mineralized hydroxyapatite coated on titanium alloy for biomedical applications, Mater. Today 4 (13) (2017) 12393–12400.

[34] R. Patra, B. Vijay, K.S. Raju, K. Gobi, R. Subasri, Dual functional coatings: comparative study of corrosion indicators for corrosion reporting and self-healing on MgAZ31 alloy, J. Alloys. Compd. (2025) 180755.

[35] Y. Akinay, E. Karatas, D. Ruzgar, A. Akbari, D. Baskin, T. Cetin, H.C. Kazici, M. Topuz, Cytotoxicity and antibacterial activity of polyhedral oligomeric silsesquioxane modified Ti3C2Tx MXene films, Sci. Rep. 15 (1) (2025) 8463.

[36] B. Ulas, T. Cetin, M. Topuz, Y. Akinay, Ti2NTx MXene materials derived from Ti2AlN MAX phases: their characterization and electrocatalytic activity toward hydrazine electrooxidation, Int. J. Hydrog. Energ. 82 (2024) 892–900.

[37] N. Asadi, R. Naderi, M. Mahdavian, Halloysite nanotubes loaded with imidazole dicarboxylic acid to enhance protection properties of a polymer coating, Prog. Org. Coat. 127 (2019) 375–384.

[38] B.C. Leal, J.D. Scholten, M.C. Alves, J. Morais, I. De Pedro, L. Fernandez Barquin, J. Dupont, Interacting superparamagnetic iron (II) oxide nanoparticles: synthesis and characterization in ionic liquids, Inorg. Chem. 55 (2) (2016) 865–870.

[39] R. Haldhar, C.J. Raorane, V. Mishra, T. Periyasamy, A. Berisha, S.C. Kim, Development of different chain lengths ionic liquids as green corrosion inhibitors for oil and gas industries: experimental and theoretical investigations, J. Mol. Liq. 372 (2023) 121168.

[40] P. Gogoi, K. Boruah, R. Borah, Synthesis of triethylamine-bridged basic tricationic ionic liquids and evaluation of their catalytic efficiencies for preparation of arylidene or alkylidenemalononitrile, ChemistrySelect. 3 (32) (2018) 9476–9483.

[41] N. Anita, R. Joany, R. Dorothy, J. Aslam, S. Rajendran, A. Subramania, G. Singh, C. Verma, Linear Polarization Resistance (LPR) Technique For Corrosion measurements, Electrochemical and Analytical Techniques For Sustainable Corrosion Monitoring, Elsevier, 2023, pp. 59–80.

[42] E. Saccullo, V. Patamia, A. Bifarella, A. Ferlazzo, R. Fiorenza, L. Spitaleri, G. Sfuncia, G. Nicotra, C. Zagni, M.T.A. Iapichino, Conversion of VOC-derived CO2 into sustainable products with a natural magnetic alginate composite, Int. J. Biol. Macromol. (2025) 140695.

[43] J. Matthew, Surface analysis by Auger and x-ray photoelectron spectroscopy, in: D. Briggs, J.T. Grant (Eds.), IMPublications, Chichester, UK and SurfaceSpectra, Wiley Online Library, Manchester, UK, 2003, p. 900. ISBN 1-901019-04-7, 900 pp2004.

[44] A. Gulino, Structural and electronic characterization of self-assembled molecular nanoarchitectures by X-ray photoelectron spectroscopy, Anal. Bioanal. Chem. 405 (2013) 1479–1495.

[45] G. Greczynski, L. Hultman, Compromising science by ignorant instrument calibration—need to revisit half a century of published XPS data, Angew. Chem. 132 (13) (2020) 5034–5038.

[46] L. Spitaleri, C.M. Gangemi, R. Purrello, G. Nicotra, G. Trusso Sfrazzetto, G. Casella, M. Casarin, A. Gulino, Covalently conjugated gold–porphyrin nanostructures, Nanomaterials 10 (9) (2020) 1644.

[47] Z. Terzopoulou, D.G. Papageorgiou, G.Z. Papageorgiou, D.N. Bikiaris, Effect of surface functionalization of halloysite nanotubes on synthesis and thermal properties of poly(ε-caprolactone), J. Mater. Sci. 53 (9) (2018) 6519–6541.

[48] A. Ferlazzo, M.T. Armeli Iapichino, G. Calabrese, G. D'Accurso, R. Fiorenza, V. Pistarà, A. Gulino, A. Rescifina, V. Patamia, G. Floresta, Nanosensors made of halloysite and Kojic acid metal complexes for dopamine detection, ACS. Appl. Nano Mater. (2025).

[49] C. Duce, S. Vecchio Ciprioti, L. Ghezzi, V. Ierardi, M.R. Tinè, Thermal behavior study of pristine and modified halloysite nanotubes, J. Therm. Anal. Calorim. 121 (3) (2015) 1011–1019.

[50] W.q. Feng, Y.h. Lu, Y. Chen, Y.w. Lu, T. Yang, Thermal stability of imidazolium-based ionic liquids investigated by TG and FTIR techniques, J. Therm. Anal. Calorim. 125 (2016) 143–154.

[51] V. Patamia, D. Gentile, R. Fiorenza, V. Muccilli, P.G. Mineo, S. Scirè, A. Rescifina, Nanosponges based on self-assembled starfish-shaped cucurbit [6]urils functionalized with imidazolium arms, Chem. Commun. 57 (30) (2021) 3664–3667.

[52] V. Vergaro, E. Abdullayev, Y.M. Lvov, A. Zeitoun, R. Cingolani, R. Rinaldi, S. Leporatti, Cytocompatibility and uptake of halloysite clay nanotubes, Biomacromolecules 11 (3) (2010) 820–826.

[53] O.P. Setter, E. Segal, Halloysite nanotubes–the nano-bio interface, Nanoscale 12 (46) (2020) 23444–23460.

[54] T. Wang, Y. Chen, C. Hou, X. Qiao, PEG-modified halloysite as a hydrophilic interaction and cation exchange mixed-mode sorbent for solid-phase extraction of biogenic amines in fish samples, Anal. Bioanal. Chem. 415 (18) (2023) 4265–4275.

[55] G. Cavallaro, S. Milioto, S. Konnova, G.l. Fakhrullina, F. Akhatova, G. Lazzara, R. Fakhrullin, Y. Lvov, Halloysite/keratin nanocomposite for human hair photoprotection coating, ACS. Appl. Mater. Interfaces. 12 (21) (2020) 24348–24362.

[56] B. Katana, D. Takács, A. Szerlauth, S. Sáringer, G. Varga, A. Jamnik, F.D. Bobbink, P.J. Dyson, I. Szilagyi, Aggregation of halloysite nanotubes in the presence of multivalent ions and ionic liquids, Langmuir 37 (40) (2021) 11869–11879.

[57] S.N. Pedro, C.S. Freire, A.J. Silvestre, M.G. Freire, Ionic liquids in drug delivery, Encyclopedia 1 (2) (2021) 324–339.

[58] Z. Yadollahi, M. Motiei, N. Kazantseva, J. Císař, P. Sáha, Whey protein isolate-chitosan polyelectrolyte nanoparticles as a drug delivery system, Molecules 28 (4) (2023) 1724.

[59] C.L. Domínguez-Delgado, Z. Akhtar, G. Awuah-Mensah, B. Wu, H.D.C. Smyth, Effects of process and formulation parameters on submicron polymeric particles produced by a rapid emulsion-diffusion method, Nanomaterials 12 (2) (2022) 229.

[60] Y. Zou, J. Wang, Y. Zheng, Electrochemical techniques for determining corrosion rate of rusted steel in seawater, Corros. Sci. 53 (1) (2011) 208–216.

[61] M.A. Amin, M. Ahmed, H. Arida, F. Kandemirli, M. Saracoglu, T. Arslan, M. A. Basaran, Monitoring corrosion and corrosion control of iron in HCl by non-ionic surfactants of the TRITON-X series–Part III. Immersion time effects and theoretical studies, Corros. Sci. 53 (5) (2011) 1895–1909.

[62] K. Ansari, M. Quraishi, A. Singh, Schiff's base of pyridyl substituted triazoles as new and effective corrosion inhibitors for mild steel in hydrochloric acid solution, Corros. Sci. 79 (2014) 5–15.

[63] C. Verma, M. Quraishi, I. Obot, E.E. Ebenso, Effect of substituent dependent molecular structure on anti-corrosive behavior of one-pot multicomponent synthesized pyrimido [2, 1-B] benzothiazoles: computer modelling supported experimental studies, J. Mol. Liq. 287 (2019) 110972.

[64] E. de Britto Policarpi, A. Spinelli, Application of Hymenaea stigonocarpa fruit shell extract as eco-friendly corrosion inhibitor for steel in sulfuric acid, J. Taiwan. Inst. Chem. Eng. 116 (2020) 215–222.

[65] A.K. Singh, A.A. Mansour, M. Singh, S. Thakur, B. Pani, R. Salghi, Relation of alkyl chain length and corrosion inhibition efficiency of N-Acylated Chitosans over mild steel in acidic medium, J. Environ. Chem. Eng. (2024) 113179.